Journal of
Ceramic Science
and Technology

J. Ceram. Sci. Tech., **06** [03] 221-230 (2015)
DOI: 10.4416/JCST2015-00005
available online at: http://www.ceramic-science.com

A Study on the Polymer Precursor Formation and Microstructure Evolution of Square-Shaped $(La_{0.5}Ba_{0.5})(Mn_{0.5}Fe_{0.5})O_3$ Ceramic Nanoparticles

M. Romero[1, 2], H. Pardo[*1, 2], R. Faccio[1, 2], L. Suescun[1, 2], S. Vázquez[1], I. Laborda[1], L. Fernández-Werner[1, 2], Á. Acosta[3], J. Castiglioni[4],Á.W. Mombrú[1, 2]

[1]Cryssmat-Lab/Centro NanoMat – DETEMA – Facultad de Química – Universidad de la República – P.O. Box 1157, Montevideo, URUGUAY.
[2]Centro Interdisciplinario de Nanotecnología, Química y Física de Materiales – Espacio Interdisciplinario – Universidad de la República – P.O. Box 1157, Montevideo, URUGUAY.
[3]Cátedra de Química Inorgánica, DEC, Facultad de Química, Universidad de la República – P.O. Box 1157, Montevideo, URUGUAY.
[4]Cátedra de Fisicoquímica, DETEMA, Facultad de Química, Universidad de la República – P.O. Box 1157, Montevideo, URUGUAY.

received January 23, 2015; received in revised form March 1, 2015; accepted March 10, 2015

Abstract

The polymer precursor formation and the growth mechanism of $(La_{0.5}Ba_{0.5})(Mn_{0.5}Fe_{0.5})O_3$ ceramic nanoparticles have been studied. First, we focused on the influence of isolated metals (La, Ba, Mn, Fe) on the polymer precursor formation by means of Raman, FT-IR, scanning electron microscopy and differential scanning calorimetry, showing that the presence of metal ions, especially iron, increases the oxidation rate of the polymer precursor, while the presence of barium leads to a higher degree of polymerization, preventing partial oxidation of the polymer at low temperatures and allowing the presence of nitrates at the combustion stage. Nevertheless, when all metals are present, the polymer precursor showed a largely homogeneous microstructure with a global average influence from all cations.

Finally, we studied the microstructure evolution of nanoparticles obtained after calcination above 700 °C. SAXS and TEM analysis suggests that the formation of square-shaped nanoparticles below 900 °C and coalescence leads to the formation of larger-sized and round-shaped nanoparticles at 900 °C.

Keywords: SAXS, perovskite, nanoparticle, sol-gel, polymer precursor.

I. Introduction

Manganites [1–3] and iron-based perovskites [4–6] have been studied in recent years in order to obtain fundamental and applied knowledge from the physical properties that they exhibit. Additionally, iron-substituted manganites ($Ln_{1-Y}Ba_YMn_{1-X}Fe_XO_3$ with Ln = lanthanides) have been studied because of their potential application as oxidation catalysts. There is strong evidence that Fe-doped manganites show an enhancement of catalytic activity of this oxide [7, 8].

In order to obtain ceramic nanoparticles, the most commonly synthesis techniques used are gel-combustion [9] and the polymer precursor method [10, 11]. For the purposes of this paper, we have selected the polymer precursor method to prepare quaternary perovskite $(La_{0.5}Ba_{0.5})(Mn_{0.5}Fe_{0.5})O_3$. The Pechini method is based on *in-situ* polymerization of a polyol and a multifunctional carboxylic acid, which plays the role of chelating and esterification agent [12]. Ethylene glycol is commonly used as the polyol and citric acid as carboxylic acid because its three carboxylic groups enhance its chelating ability.

In the particular case of multicomponent perovskites it is very difficult to obtain strict control of the synthesis using these "wet chemistry" methods. This is mainly attributed to the different solubility and stability of the metal-citrate complexes in solution. Particular caution must be taken with barium nitrate, because of its low solubility and the relative low stability of barium-citrate complexes [13].

The thermal stability of citrate and the presence of metal cations during the reaction are important aspects during the gelation process. Besides, the dehydration process leading to aconitate is favored when the acidity of the citrate hydroxyls is high [14–17]. In spite of some suggestions about the use of carbonates [18], nitrates lead to a thorough combustion owing to the oxidizing character of these anions. There are reports that transition metals such as iron and manganese are good catalysts for the oxidation of citrate by nitrates, not only in the combustion conditions but also at lower temperatures [19].

* Corresponding author: hpardo@fq.edu.uy

The nature of the metal in solution has a significant influence in the gelification and esterification kinetics since the presence of metals in solution increases the rate in the gelification process [20].

The selection of the optimal ratio between citrate and ethylene glycol is also very relevant and case-sensitive. According to the bibliography [21], excess of ethylene glycol and high temperature, or excess of citrate and low temperatures are adequate conditions for reactions. Although the high viscosity due to the excess of ethylene glycol prevents the segregation of salts, high temperature could yield the decomposition of citrate, so both alternatives should be considered.

The nitrate-to-citrate ratio is also important in the combustion process, since it determines a complete combustion of the polymeric gel in one step, ensuring kinetic control to obtain small nanoparticles. A relative high heating rate at this stage is also one key to preventing the formation of thermodynamically stable intermediates such as carbonates [20–25].

Nevertheless, less attention has been given to the effect of constitutive metals in the polymer precursor and the consequences for the nanoparticles' microstructure after thermal treatment. The small-angle x-ray scattering (SAXS) technique has been widely used to characterize materials such as polymers, oxide nanoparticles, and more recently, the microstructure evolution mechanism during the calcination of oxide nanoparticles [26–28]. Up to now, to our knowledge, there are very few reports [11] on SAXS studies evaluating the microstructure evolution in the synthesis of nanoparticles by means of the polymer precursor method.

In this report we present a detailed study on the synthesis of perovskite nanoparticles with the polymer precursor method, discussing the influence of metals on the polymer precursor, the formation mechanism and the consequences for the microstructure evolution of $(La_{0.5}Ba_{0.5})(Mn_{0.5}Fe_{0.5})O_3$ perovskite nanoparticles.

II. Experimental

Analytical-grade lanthanum nitrate ($La(NO_3)_3.6H_2O$; Sigma Aldrich 99.99 %), barium nitrate ($Ba(NO_3)_2$; Sigma Aldrich > 99 %), manganese nitrate ($Mn(NO_3)_2.4H_2O$; Sigma Aldrich 99 %), ferric nitrate ($Fe(NO_3)_3.9H_2O$; Sigma Aldrich 99.99 %), ethylene glycol ($C_2H_6O_2$) and citric acid ($C_6H_8O_7.H_2O$) were used as starting materials. Each metal nitrate (M) and citric acid (CA) was dissolved in deionized water in a M:CA:H_2O molar ratio equal to 1:3:100 and stirred separately for 2 h at 50 °C with M = La, Ba, Mn and Fe. Ethylene glycol (EG) was added to each solution as well as to the mixed solution in a CA:EG molar ratio equal to 1:2 and dropwise addition of ammonia was needed to adjust pH = 3–4. All precursor samples were named pM-T(t) with M = La, Ba, Mn, Fe (for each metal precursor), LBMFO (for synthesis precursor), T for temperature and t for time of heating. The solutions were heated at 100 °C for 6 h to form all pM-100(6) polymer precursors.

The polymer precursor of synthesis pLBMFO-100(6) was heated at 700 °C, 800 °C, and 900 °C for 4 h using a 10 °K/min rate to obtain nanocrystalline $(La_{0.5}Ba_{0.5})(Mn_{0.5}Fe_{0.5})O_3$ samples named LBMFO-T, using T for temperature of heating.

Raman spectroscopy was used to study *in-situ* polymerization stage in pM-100(t) samples with t = 0, 3, 6 h using a DeltaNu Advance 532 spectrometer with a 532 nm laser wavelength and 20mW power using glass vials in the range of 200 – 3400 cm^{-1} by averaging 30 scans with a resolution of 3 cm^{-1} for each spectrum with total integration time of 300 s. Only fluorescence correction was performed on the raw data using DeltaNu Advance Software. pM-100(6) samples were also analyzed by means of FT-IR spectroscopy using a Shimadzu Prestige 21 FT-IR in 3 % KBr pellets in the range of 400 – 4000 cm^{-1} by averaging 30 scans with a resolution of 3 cm^{-1} for each spectrum.

In order to assign the vibrational modes of experimental data we calculated Raman and Infrared spectra for nitrate ion, citric acid (CA), ethylene glycol (EG) and a reference monomer of two ethylene glycol linked via ester to terminal carboxyl groups of citric acid (EG-CA-EG). We performed quantum chemical calculations using density functional theory (DFT) [29,30] using the hybrid exchange-correlation potential B3LYP [31–34] at 6 – 311+G(d,p) level of theory as implemented in Gaussian 09 [35].

Elemental analysis was performed using Elemental Analyzer Carlo Erba Model 1108. Thermal decomposition was analyzed by Differential Scanning Calorimetry (DSC) and thermogravimetric analysis (TGA) using Shimadzu DSC-60 and TGA using Shimadzu TGA-50, respectively. Both analyses were performed at 50 mL/min air flow and a heating rate of 10 °K/min between 30 – 600 °C. DSC measurements were additionally performed on sealed aluminum crimps in order to observe more clearly thermal decomposition avoiding the ethylene glycol excess evaporation. pM-100(6) and nanocrystalline powder were also observed in a JEOL JSM-5900LV scanning electron microscope (SEM) in the secondary electron imaging mode (SEI) and in the backscattered electron composition (BEC) imaging mode with EDS analysis. x-ray powder diffraction (XRPD) was performed using a Rigaku Ultima IV diffractometer with CuKα radiation in the range 2θ = 10 – 70° in 2θ scanning for 2 s every 0.02 degrees. Small angle x-ray scattering (SAXS) experiments were performed using a Rigaku Ultima IV diffractometer with CuKα radiation in q scattering vector range of 0.08 – 4.00 $Å^{-1}$ analyzed with the three-region Guinier-Porod model [36].

The Guinier part of the I(q) versus q curve implemented in the low- and mid-q region in this model is given by the following equations:

$$I(q) = \frac{G_1}{q^{S1}} e^{\frac{-q^2 R_{G1}^2}{3-S_1}} \text{ (at low-q region)} \quad (1)$$

$$I(q) = \frac{G_2}{q^{S2}} e^{\frac{-q^2 R_{G2}^2}{3-S_2}} \text{ (at mid-q region)} \quad (2)$$

where G_i is a Guinier scale factor, R_g is the gyration radius and the parameter S_i is a parameter included to model non-spherical objects being $S_i = 2$ for lamellae or platelets, $S_i = 1$ for rods and $S_i = 0$ for spheres. In the three region model, for randomly oriented lamellae of thickness (T) with equal width and length (W = L), $R_{g1} = (W^2/12 + T^2/12)^{1/2}$ and

$R_{g2} = T/12^{1/2}$ using $S_1 = 0$ and $S_2 = 2$ in Eq. 1 and 2, respectively. On the other hand, for a sphere with radius (R), the gyration radius of is $R_g = R(3/5)^{1/2}$. SAXS analysis can be employed to study the fractal structures employing power-law regions in which the intensity I(q) may show an exponential dependence on q as shown in Eq. 3.

$$I(q) = A\, q^{-P} \quad (3)$$

where P is the Porod exponent and A is a Porod scale factor.

The value of the Porod exponent (P) gives the dimensionality of the scattering object in which mass fractals (D_M) and surface fractals (D_S) dimensions are given in the following equations:

$0 < p < 2$ for mass fractal, $D_M = P + 1$
$2 < p < 3$ for surface fractal, $D_S = 6 - (P + 1)$
$P > 3$ for non-fractal [36].

Nanoparticles were observed at 100 kV using a JEOL JEM 1010 transmission electron microscope (TEM) equipped with a Hamamatsu C-4742–95 camera. The powder was dispersed in isopropyl alcohol and sonicated for 10 min. A 5 μL drop of the solution was deposited onto a holey carbon film.

III. Results and Discussion

(1) Effect of metal on the pLBMFO-100(6) polymer precursor formation

(a) *Raman and FT-IR analysis*

A strong peak in all pM-100(t) Raman spectra (Fig. 1) at ~ 1052 cm^{-1} due to symmetric stretching of nitrate was observed. All samples except pBa-100(t) showed a progressive decrease of nitrate peak with increasing time, mostly for pFe-100(t) sample, probably due to its consumption on the oxidation of ethylene glycol and citrate. It is well known that many metals, but especially iron, play an important role as a catalyst in the oxidation of organic compounds. Furthermore, all samples and mostly pBa-100(t) showed a progressive Raman shift from 1052 to 1046 cm^{-1} with increasing time, suggesting partial formation of nitrate-to-metal links [37,38] as the evaporation of water takes place. In pBa-100(t), both the constant intensity and the shift towards lower wavenumber are mainly attributed to the higher stability of barium nitrate in comparison with the other cations.

Raman analysis suggested the linkage between citrate and ethylene glycol for all pM-100(6) samples compared to free ethylene glycol and citric acid, evidenced by Raman shifts from 750 to 780–800 cm^{-1}, is probably due to central citrate carbonyl ν(C-C) stretching, 860 to 885–910 cm^{-1} probably due to ethylene glycol ν(C-O) stretching, 937 to 950–960 cm^{-1} probably due to citrate terminal carbonyl ν(C-C) stretching. All vibrational modes observed experimentally were assigned by theoretical calculations and are listed in Table 1.

FT-IR spectra of pM-100(6) samples (Fig. 2) showed a shift in the ethylene glycol ν(C-O) from 1063 to 1080–1085 cm^{-1} due to esterification but in pFe-100(6) the intensity of this vibrational mode is less intense than in the other samples, in agreement with the higher oxidation ascribed to its catalyst behavior. Another shift was observed in the citrate terminal carbonyl stretching mode from 1155 to 1175–1200 cm^{-1} due to esterification [40]. Evidence of metal coordination in all samples could be assigned by two peaks at 1430–1450 and 1600–1650 cm^{-1} probably attributed to the asymmetric and symmetric stretching vibrations, respectively, of unidentate and bidentate carboxylate groups [40–42]. Nevertheless, this assumption is affected by the δH_2O overlapping at 1640 cm^{-1} in both Raman and FT-IR spectra. The symmetric stretching of terminal and central carbonyl groups ν(O=C=O) are seen at 1724–1730 cm^{-1} and 1735–1755 cm^{-1}, respectively, appearing as a broad single band centered at 1720–1740 cm^{-1}, as observed previously for this polyester [43–47]. In pFe-100(6) sample, a noticeable decrease in the intensity of C-O stretching modes of ethylene glycol at 888 cm^{-1} and 1080 cm^{-1} accompanied by a slight increase in the C=O stretching modes at 1724 cm^{-1} suggested oxidation of ethylene glycol probably to form glycolaldehyde or glycolic acid [48] and partial ketonic decarboxylation of citric acid to form acetoacetic ester [49]. pLBMFO-100(6) showed all vibrational modes corresponding to the polyester formation as observed and discussed for isolated pM-150 spectra, with a particular similarity with M = Ba and Mn spectra. Regarding on this observations, it could be assumed that the presence of barium and manganese in these polymer precursors will tend to form higher-polymerized and homogeneous microstructures while the presence of lanthanum and specially iron, to form lower-polymerized and inhomogeneous microstructures.

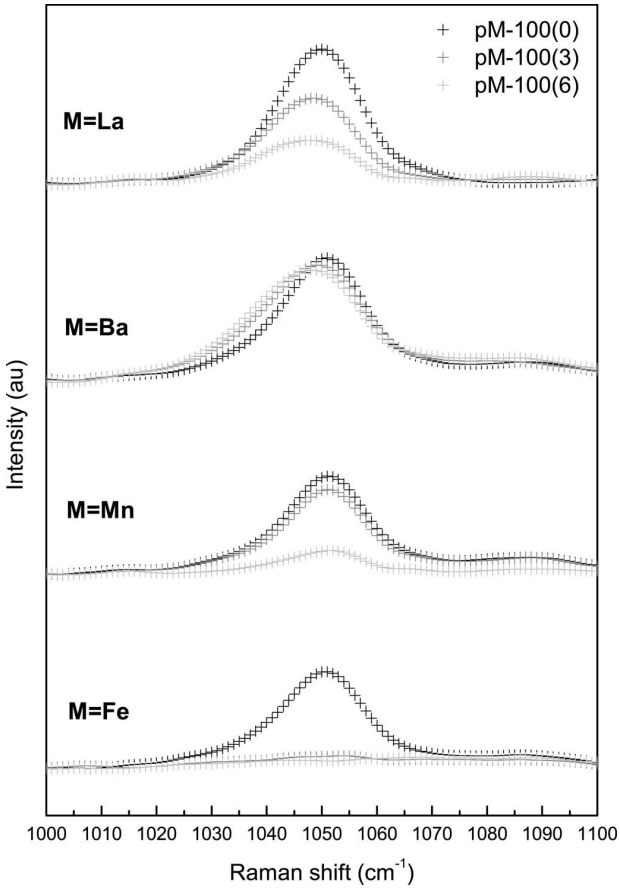

Fig. 1: Raman nitrate stretching peak of pM-100(t) with t =0, 3 and 6 h.

Table 1: Observed frequencies in infrared (I) and Raman (R) spectra for pM-100(6) in cm^{-1} and assignation based in NO^-_3, CA, EG and EG-CA-EG monomer theoretical calculation (*).

	NO^-_3*	CA*	EG*	EG-CA-EG*	pLa-100(6)	pBa-100(6)	pMn-100(6)	pFe-100(6)
π(OH)-CA central	-	586s (I)	-	664s (I)	661s (I)	663m (I)	667s (I)	663m (I)
γ(C-C-O)-CA	-	708s (I)	-	774s (I)	792s (I)	779w (I)	793w, 813w (I)	785w, 809w (I)
ν(C-C)-CA central	-	754s (R)	-	780s (R)	796s (R)	797vw, 811vw (R)	783w, 813w (R)	779w, 800w (R)
ν(C-O)-EG	-	-	843s (R,I)	862s (R-I)	868s (R) 841s (I) 896s (R) 893s (I)	872vw (R) 885s (R)	870w (R) 877w (I) 882w (R) 889s (I)	870m (R) 879m (I) –
ν(C-C)-CA terminal	-	937s (R)	-	937s (R) 937s (I)	955s (R) 958w (I)	951s (R)	952s (R)	947s (R)
ν(C-O)-CA hydroxyl	-	-	988w (R,I)	976w (R)	979m (R) 977m (I)	979w (R) 976m (I)	978w (I)	975w (I)
ν(N=O)-NO_3	1073vs (R)	-	-	-	1046vs (R)	1046vs (R)	1053m (R)	1049w (R)
ν_{as}(C-O)-EG	-	-	1063s (I)	1094s (R) 1094s (I)	1088s (R) 1080s (I)	1090s (R) 1082s (I)	1092m (R) 1082m (I)	1090m (R) 1080m (I)
ν(C-OH)-CA central	-	1132m (R,I)	-	1134m (R) 1131m (I)	1142m (R) 1122m (I)	1137m (R) 1122m (I)	1138w (R) 1124w (I)	1133w (R) 1122w (I)
ν(C-O)-CA terminal	-	1155s (I)	-	1175s (I)	1180s (I)	1181s (I)	1198s (I)	1176s (I)
π(CH2)-EG	-	-	1185m (R,I)					
ν(C-OH)-CA central	-	1200w (R,I)	-	1256w (R,I)	1288w (R)	1242w (R-I)	1252w (I)	1264w (R) 1250w (I)
ν(N=O)-NO_3	1339s (I)	-	-	-	1388m (I)	1385m (I)	1385s (I)	1385w (I)
δ(C-O-H)-CA		1345m (R)		1391m (R)				
wag(CH2)-CA	-	1395s (R) 1395s (I)	-	1483vw (R)	1403m (R)	1403m (R)	1398m (R)	1398m (R)
π(CH2)-EG	-	-	1360m (R)	1404m (R)				
π(CH2)-CA	-	1306vw (R)	-	1416m (R)	1415m (R)	1413m (R)	1412m (R)	1418m (R)
δ_s(C-O-H)-CA	-	1401m (R)	-	1437w (R)	1430m (R)	1424m (R)	1426m (R)	1426m (R)
π(CH2)-EG	-	-	1411m (R)	1456s (R)	1464s (R)	1468s (R)	1467m (R)	1469m (R)
ν_{as}(COO^-)-CA	-	1450m (I)	-	-	~1452m (I)	~1436m (I)	~1427m (I)	~1429s (I)
ν_s(COO^-)-CA	-	1745m (I)	-	-	~1614m (I)	~1610mw (I)	~1624mw (I)	~1640m (I)
ν(C=O)-CA terminal	-	1811s (R)	-	1845s (R)	1730m (R)	1730m (R)	1724m (R)	1724s (R)
ν(C=O)-CA central	-	1835s (R)	-	1858s (R)	1751m (R)	1752m (R)	1735m (R)	1735s (R)

Assignments are as follows: ν (stretching), δ (scissoring), π (twisting), γ (out-of plane deformation), wag (wagging), s (strong), m (middle), w (weak).

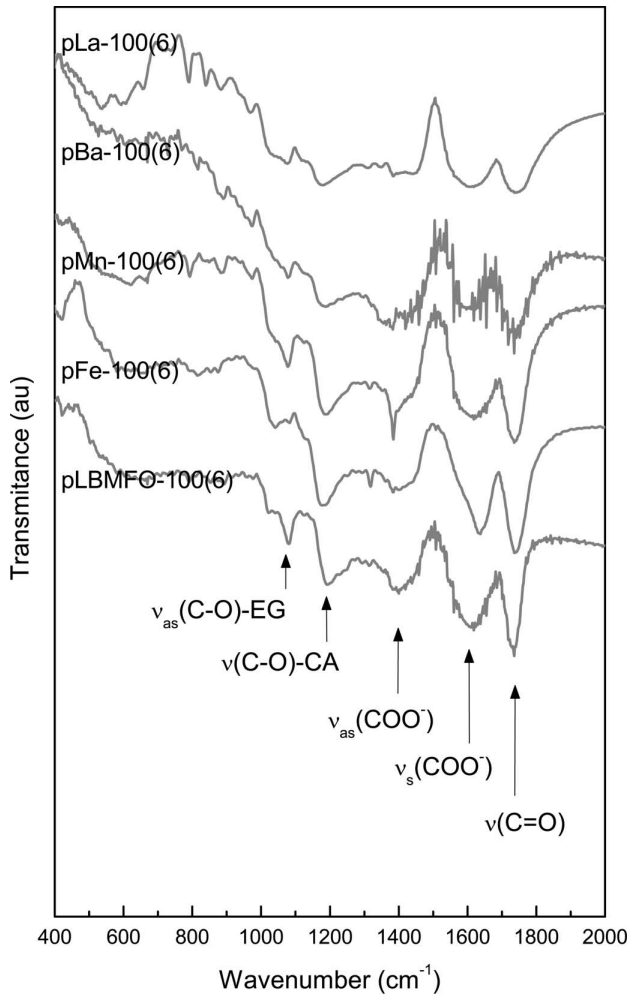

Fig. 2: FT-IR spectra of pM-100(6) samples with M = La, Ba, Mn, Fe and LBMFO.

(b) ***SEM and EDS analysis***

SEM images related to all pM-100(6) samples precursors show (Fig. 3) a polymer-like feature evidenced by a typical morphology consistent in bidimensional layers. In the case of pLa-100(6), pBa-100(6) and pMn-100(6), the layer thickness appeared to be higher than in pFe-100(6) samples. On the other hand, especially in pFe-100(6) sample the layers appeared to be smaller and more exfoliated, which could be in agreement with a poor level of polymerization owing to the oxidation process as discussed previously. pLBMFO-100(6) showed the same layered polymeric-type structure as observed for isolated samples and no evidence of local decomposition was observed, suggesting that this precursor did not behave as simply the sum of all isolated precursors. EDS analysis confirmed the presence of all metallic species in a good homogeneous distribution in the polymeric precursor. When all metals are present, it could be assumed that the polymer precursor, instead of being formed by different layers of the isolated precursors, is formed by homogeneous layers having an average of all isolated precursors' level of polymerization with a well-defined intermediate microstructure.

(c) ***DSC and TGA analysis***

DSC, performed on air flow condition, showed no significant evidence of citrate decomposition or citrate-ethylene glycol polyester below 300 °C (Fig. 4a) probably hidden because of the broad peak related to ethylene glycol evaporation [50]. For this reason, DSC performed on sealed aluminum crimps (Fig. 4a-inset) were used in order to observe thermal decomposition below 300 °C avoiding this broad endothermic peak.

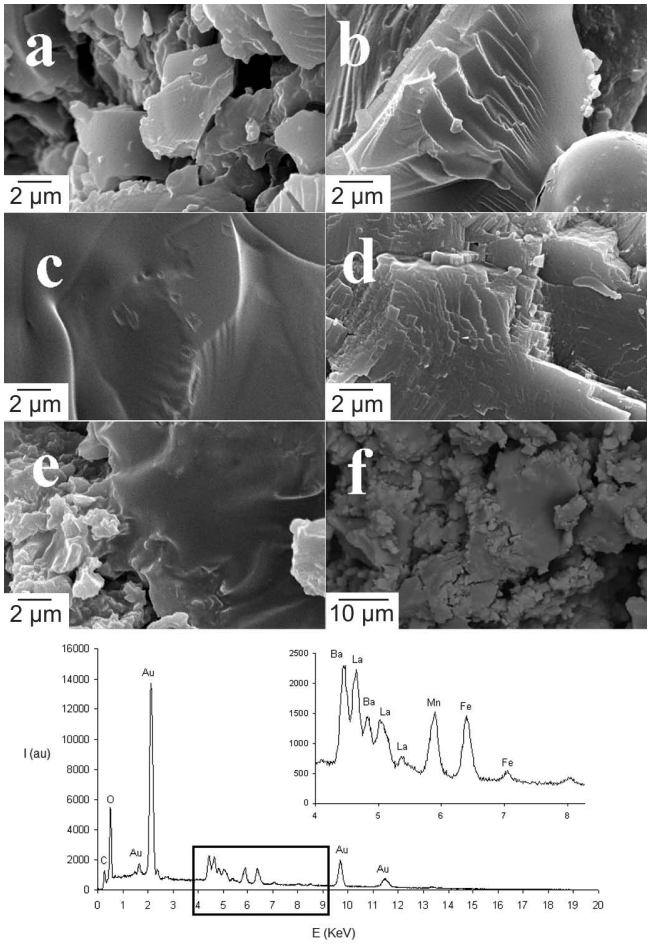

Fig. 3: SEM images for pM-100(6) with M = La (a), Ba (b), Mn (c), Fe (d) and LBMFO on secondary electron imaging SEI (e) and backscattered electron collection mode BEC (f) with EDS analysis.

pLBMFO-100(6) showed an endothermic peak at ~ 223 °C attributed to the dehydratation and decarboxylation of the polymer precursor resin. pLa-100(6) and pBa-100(6) samples showed an endothermic peak at higher temperatures (240 – 255 °C), suggesting a high level of polymerization while pFe-100(6) and pMn-100(6) samples showed lower temperatures of decarboxylation (T = 180 – 230 °C). This is probably due to the minor level of coordination of higher size ions with citrate carboxylates, especially Barium, and the consequently major number of free citrate carboxylates to form more ester links with ethylene glycol. This observation suggests an intermediate level of polymerization in comparison to isolated precursors and allows us to argue that the pLBMFO-100(6) system did not polymerize as simply the sum of individual pM-100(6) samples because there is only one endothermic peak, also suggesting good homogeneity of the dry precursor.

DSC performed on air flow conditions showed that combustion of pLBMFO-100(6) took place at 450 – 500 °C in

a single exothermic step as usually observed for highly homogeneous polymer precursors [39]. pLa-100(6), pMn-100(6) and pFe-100(6) combustion was observed at 400 – 520 °C, 370 – 400 °C and 270 – 430 °C, respectively, and no combustion process was observed until 600 °C for the pBa-100(6) sample. Temperature of combustion of pLBMFO-100(6) polymer precursor showed an intermediate temperature of combustion in comparison with all isolated pM-100(6) precursors, also suggesting that the pLBMFO-100(6) chemical structure is not the simply the sum of all isolated precursors with M=La, Ba, Mn and Fe, but that a global average influence from all of them is observed.

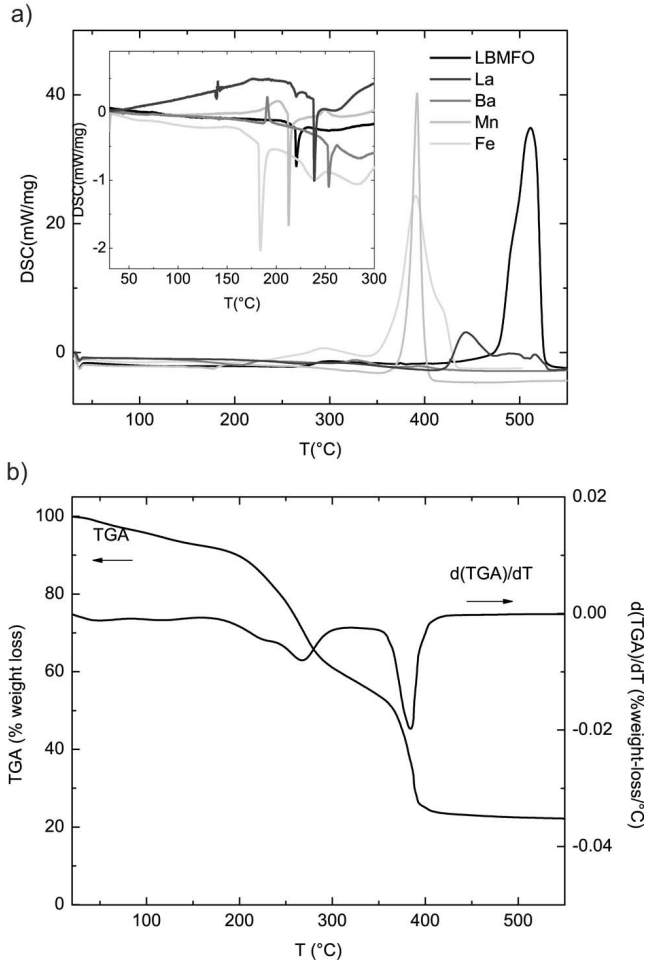

Fig. 4: a) DSC performed in open and sealed (inset) aluminum crimps and **b)** TGA-DrTGA for pM-100(6) with M = La, Ba, Mn, Fe, LBMFO.

TGA performed on this sample (Fig. 4b) showed a weight loss of about 10 % below 150 °C, which is probably due to humidity; and a 20 % weight loss between 180 – 300 °C probably due to ethylene glycol excess evaporation and citrate partial decarboxylation and total decomposition of organic matter at approximately 400 °C with a weight loss of 40 %.

Elemental analysis showed a decrease in the weight fraction of nitrogen for all samples when compared to initial molar ratios. This fact is also in accordance with partial oxidation of ethylene glycol and citrate, especially in pLa-100(6) and pFe-100(6) samples, in which the nitrogen content was close to zero. pLBMFO-100(6) sample elemental analysis also evidenced a partial oxidation of the polyester and it could be assumed that it is due to the presence of lanthanum and mostly iron in the polymer precursor.

(2) Effect of polymer precursor on the microstructure evolution of LBMFO-T nanoparticles.

(a) *XRPD analysis*

XRPD analysis (Fig. 5) of pLBMFO-100(6) sample confirmed the presence of a highly amorphous polymer showing only a very wide peak centered at $2\theta \sim 23°$ due to very small-sized nanocrystalline polyester. The formation of nanocrystalline perovskite powder is observed after direct calcination of pLBMFO-100(6) polymer precursor at 700 °C (LBMFO-700) with minor concentrations of La_2O_3, $BaCO_3$ and $LaMnO_3$ impurities that are almost totally eliminated at higher temperatures. We determined a crystallite average size following the full width at half maximum method (FWHM) obtaining 12, 19 and 23 nm for LBMFO-700, LBMFO-800 and LBMFO-900, respectively. According to XRPD characterization performed, calcinated samples below 900 °C presented detectable amounts of cubic-$LaMnO_3$, but pure $(La_{0.5}Ba_{0.5})(Mn_{0.5}Fe_{0.5})O_3$ phase is obtained without the presence of this secondary phase at 900 °C. Rietveld refinement of LBMFO-900 sample data (*not shown*) showed that $LaBaMnFeO_{6-\delta}$ compound best fitted in a tetragonal structure *P4/mmm* space group.

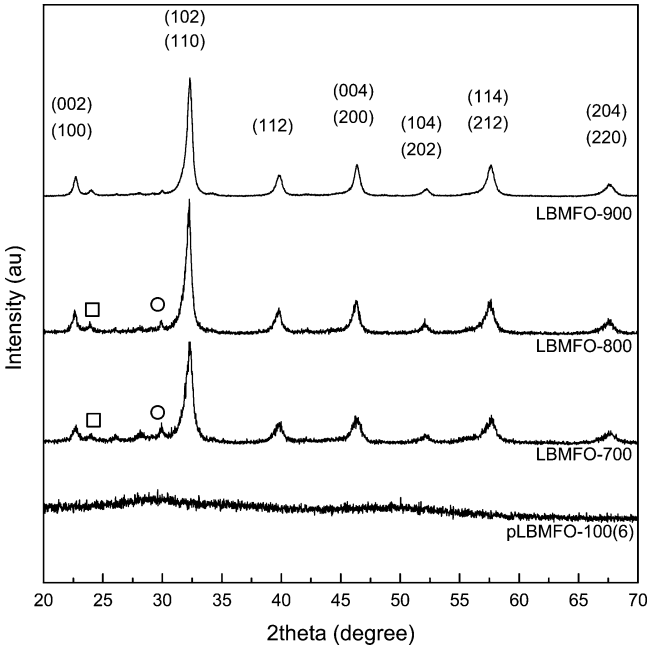

Fig. 5: x-ray powder diffraction for pLBMFO-100(6) and LBMFO-T with T = 700 °C, 800 °C and 900 °C. $BaCO_3$ and La_2O_3 impurities are marked with a square and circle, respectively.

(b) *TEM analysis*

TEM images (Fig. 6) of LBMFO-T with T = 700 and 800 °C showed the presence of nanoparticles sized between 40 – 70 nm and some larger-sized clusters. As observed in Fig. 6d and Fig. 6e, nanoparticles showed a square-like microstructure and sizes corresponding to the presence of three and four crystalline domain nanoparticles according to the crystallite size determined using

the Scherrer equation. The square-like microstructure of these nanoparticles could have its origin in the microstructure of the polymer precursor, considering that the calcination takes place in a single step with a high temperature ramp rate. This fact enables kinetic control of the synthesis of these oxide nanoparticles and the polymer precursor lamellae microstructure could serve as a template not only influencing size but also the morphology of nanoparticles obtained after its calcination. On the other hand, TEM images of LBMFO-900 showed nanocrystallites sizes of ~80 nm but also larger-sized nanoparticles with sizes ranging between ~100–150 nm and formed owing to the coalescence of smaller-sized nanoparticles. As observed in Fig. 6c and Fig. 6f, when the temperature is high enough, the larger-sized nanoparticles obtained are rounder in shape owing to the coalescence of smaller nanoparticles. At higher temperatures of calcination, coalescence between adjacent grains increases owing to the increase of the diffusion process usually following the Fick's law. This phenomenon clearly leads to the formation of larger-sized nanoparticles and also to the change in the nanoparticles' morphology. Considering that the major diffusivity is observed on the grain surfaces, this could be probably the reason that smaller square-like nanocrystals coalesce to form edge-softened, round-shaped and larger-sized nanoparticles.

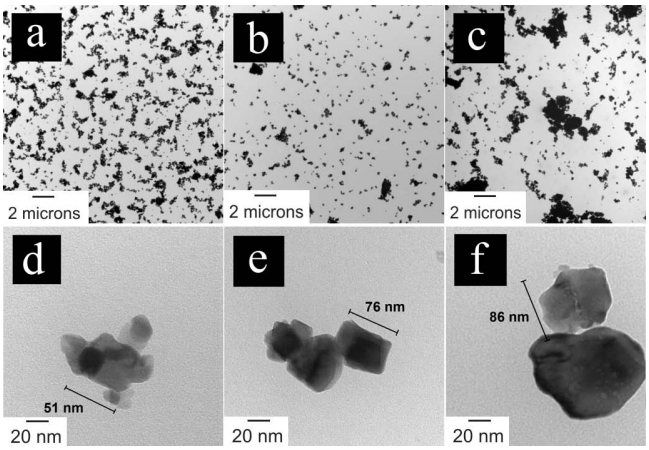

Fig. 6: TEM images for LBMFO-T with T = 700 °C (a,d), 800 °C (b,e) and 900 °C (c,f).

(c) ***SAXS analysis***

I(q) vs. q curves (Fig. 7) showed two power law regions, one at high-q region (~0.06 < q < 0.011 Å) and another at low-q region (~0.02 < q < 0.03 Å). Additionally, two broad crossover regions corresponding to the scatterers' length scales were observed at low-q region (~0.01 < q < 0.02 Å) and mid q-region (~0.03 < q < 0.06 Å). The scatterers' crossover regions were analyzed with the Guinier functions (Eq. 1 and 2) and two models were studied; a single population of lamellae particles with equal width (W) and length (L) and a different thickness (T) and a two population of spherical particles with different diameters (D_1 and D_2).

At low-q region (~0.01 < q < 0.02 Å), both spherical and lamellae models gave the same fitting statistics parameters (both models use $S_1 = 0$ in Eq. 1) but different values for diameter (D_1) and width (W=L). As observed in Table 2, spherical diameters obtained were D_1 ~ 50 nm and lamellae widths were W = L ~ 70 nm in accordance with the nanoparticles sizes observed in the TEM images (Fig. 6d-f) and especially in agreement with those values obtained for lamellae fit.

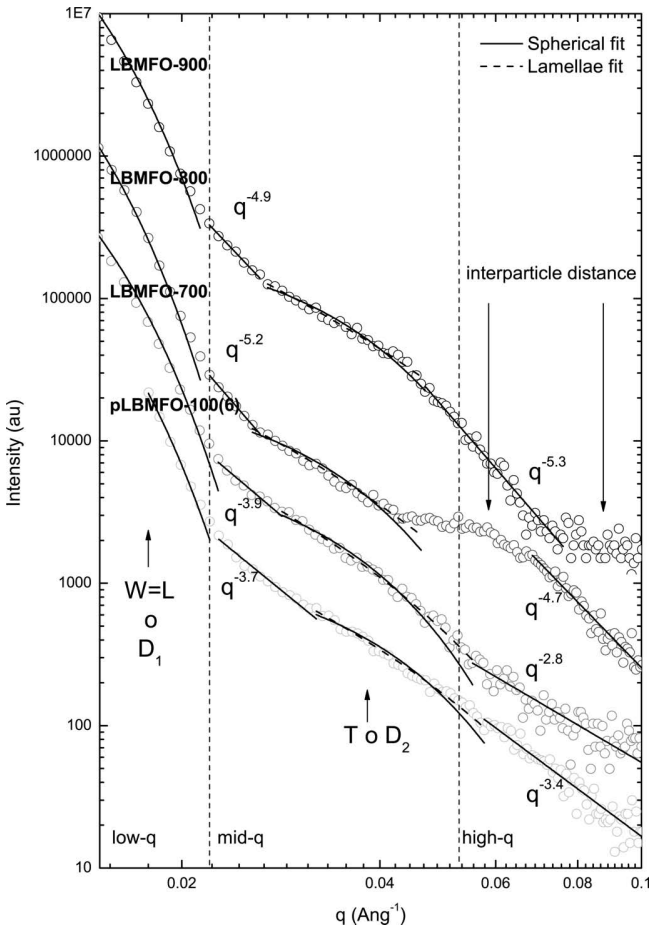

Fig. 7: I(q) vs. q plots of SAXS data and Guinier-Porod fit for pLBMFO-100(6) and LBMFO-T with T = 700 °C, 800 °C and 900 °C.

At mid-q region (0.02 < q <0.03 Å^{-1}) power law showed a ~q^{-4} dependence for all samples in accordance with the mass fractals of clusters of nanoparticles. At higher mid-q region (0.03 < q <0.06 Å^{-1}), Guinier fit using the lamellar approach ($S_2 = 2$ in Eq. 2) showed better fitting statistics parameters compared to those obtained for a new population of spherical particles ($S_2 = 0$ in Eq. 2), especially for pLBMFO-100(6) and LBMFO-700 samples. This could suggest that the mid-q region crossover is probably attributed to the thickness (T) in a lamellae model but this assumption can be hardly affected with the smoothness of the I(q) vs. q curves at mid-q region caused by the polidispersion and also with the correlation length between nanoparticles, which is typically of the same order (d ~ 3–10 nm) [27] for powder samples.

Power law observed at high-q region (~0.06 < q < 0.11 Å^{-1}) showed a ~ q^{-5} dependence for LBMFO-T with T = 800 °C and 900 °C while a ~q^{-3} dependence was observed in the case of pLBMFO-100(6) and LBMFO-700. The I(q) ~ q^{-5} dependence observed for nanoparticles obtained at higher temperatures is associated with a high sur-

face fractal owing to the smooth surface of nanocrystals. On the other hand, the I(q) ~ q^{-3} dependence observed for the polymer precursor and the nanoparticles obtained at 700 °C is associated with a D ~ 2 – 3 fractal dimension, typically observed in polymeric samples and nanoparticles with high rugosity. Two additional humps were observed for LBMFO-800 and LBMFO-900 at high-q region, ascribed to the correlation lengths between nanoparticles. These distances can be roughly estimated to be ~ $2\pi/(0.06 Å^{-1}) = 10$ nm and $2\pi/(0.1 Å^{-1}) = 6$ nm for LBMFO-800 and LBMFO-900, respectively. It is important to notice that these length scales are more likely to be ascribed to correlation lengths between nanoparticles than with a new smaller-sized population of nanoparticles, based on the fact that SAXS intensity is proportional to the electronic density contrast between the two phases and smaller-sized nanoparticles are very low-intensity scatterers.

An illustrative scheme (Fig. 8) is shown with the proposed crystal growth mechanism of $(La_{0.5}Ba_{0.5})(Mn_{0.5}Fe_{0.5})O_3$ nanoparticles. Based on all results obtained using different techniques, we observed that the polymer precursor acts as some kind of template for nanoparticles obtained after its direct calcination at lower temperatures (T = 700 – 800 °C), not only determining size but also influencing the square-shaped microstructure of these perovskite nanoparticles. At higher temperatures (T = 900 °C), coalescence of small nanoparticles tend to form larger-sized and round-shaped nanoparticles owing to coalescence between adjacent grains.

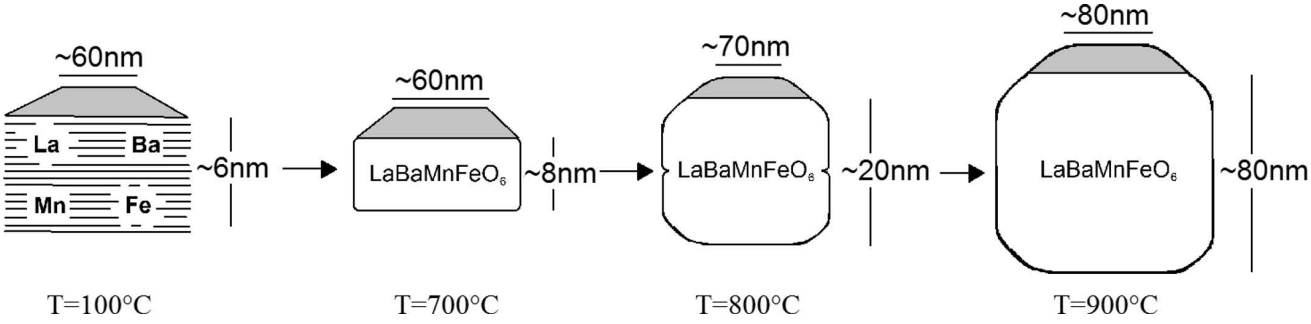

Fig. 8: Schematic showingthe proposed crystal growth mechanism of $(La_{0.5}Ba_{0.5})(Mn_{0.5}Fe_{0.5})O_3$ nanoparticles.

Table 2: Guinier-Porod fit analysis using Eqs. 1, 2 and 3 with $S_1 = 0$ and $S_2 = 2$ for the single population of lamellae particles model and $S_1 = S_2 = 0$ for the two-population of spherical particles model.

	pLBMFO100(6)	LBMFO700	LBMFO800	LBMFO900
Low-q region (~0.01<q<0.02 Å)				
Lamellae				
W=L (nm)	69.1	71.0	76.4	73.3
R^2	0.988	0.993	0.999	0.996
Spherical				
D_1 (nm)	51.5	53.0	57.1	54.6
R^2	0.988	0.993	0.999	0.996
Mid-q region (~0.02<q<0.03 Å)				
Power law (p)	3.75	3.91	5.32	4.86
R^2	0.972	0.967	0.997	0.989
Mid-q region (~0.03<q<0.06 Å)				
Lamellae				
T (nm)	6.06	7.52	6.97	7.02
R^2	0.989	0.993	0.962	0.990
Spherical				
D_2 (nm)	13.44	15.53	16.04	15.44
R^2	0.971	0.979	0.954	0.994
High-q region (~0.06<q<0.10 Å)				
Power law (p)	3.43	2.75	4.74	5.34
R^2	0.947	0.846	0.967	0.983

IV. Conclusions

$(La_{0.5}Ba_{0.5})(Mn_{0.5}Fe_{0.5})O_3$ nanoparticles were successfully synthesized with the polymer precursor method. The composition and microstructure of the polymer precursor was found to be highly influenced by the presence of different metals. Iron acts as a strong catalyst in oxidation processes of the polymer precursor, leading to a low level of polymerization. On the other hand, the presence of barium induced a high level of polymerization with no significant evidence of oxidation owing to the high stability of barium nitrate. favoring a good homogeneity of the polymer precursor in the synthesis. When all metals are present, the polymer precursor showed a largely homogeneous microstructure with a global average influence from all cations. Thermal decomposition analysis showed clear evidence of homogeneity by means of single-step combustion allowing us to obtain good purity nanoparticles above 700 °C. There is a contribution of the polymer precursor lamellar microstructure acting as some kind of template for the square-shaped nanoparticles obtained after its direct calcination at lower temperatures (T = 700 – 800 °C). At higher temperatures (T = 900 °C), nanoparticles are larger in size and more likely to have a round-shaped microstructure owing to the coalescence of smaller-sized square-shaped nanoparticles.

Acknowledgements

The authors would like to thank PEDECIBA, ANII, CSIC, INNOVA-EU and CINQUIFIMA for financial support. We should also like to express our gratitude for the financial support of ANII-POSNAC-2013 – 1-11169 PhD grant.

References

1 Cardoso, C.A., Araújo Moreira, F.M., Andreeta, M., Hernandes, A.C., Leite, E.R., De Lima, O.F., Mombrú, A.W., Faccio, R.: Physical properties of single-crystalline fibers of the colossal magnetoresistance manganite $La_{0.7}Ca_{0.3}MnO_3$, *Appl. Phys. Lett.*, **83**, 3135 – 3137, (2003).

2 Lisboa Filho, P.N., Mombrú, A.W., Pardo, H., Ortiz, W.A., Leite, E.R.: Extrinsic properties of colossal magnetoresistance samples, *Solid State Commun*., **130**, 31 – 36, (2004).

3 Lisboa Filho, P.N., Mombrú, A.W., Pardo, H., Ortiz, W.A., Leite, E.R.: Influence of processing conditions on the crystal structure and magnetic behavior of $La_{0.7}Ca_{0.3}MnO_3$ samples, *J. Phys. Chem. Solids*, **64**, 583 – 591, (2003).

4 Pardo, H., Ortiz, W.A., Araújo-Moreira, F.M., Suescun, L., Toby, B.H., Quagliata, E., Negreira, C.A., Prassides, K., Mombrú, A.W.: A new structure in the $REBaCuFeO_{5+d}$ series: $LaBaCuFeO_{5+d}$. structure and magnetic properties in the $La_{1-x}Pr_xBaCuFeO_{5+d}$ system, *Physica C*, **313**, 105 – 114, (1999).

5 Mombrú, A.W., Pardo, H., Suescun, L., Toby, B.H., Ortiz, W.A., Negreira, C.A., Araújo-Moreira, F.M.: Influence of oxygen disorder on the magnetic properties of $LaBaCuFeO_{5+d}$: An EXAFS and nêutron diffraction study, *Physica C*, **356**, 149 – 159, (2001).

6 Mombrú, A.W., Goeta, A.E., Pardo, H., Lisboa Filho, P.N., Suescun, L., Mariezcurrena, R.A., Ventura, O.N., Behak, R., Anderson, K.H., Araújo-Moreira, F.M.: Low-temperature magnetic properties of $LuBaCuFeO_{5+d}$ and $TmBaCuFeO_{5+d}$, *J. Solid State Chem*. **166**, 251 – 258, (2002).

7 Pai, M.R., Wani, B.N., Sreedhar, B., Singh, S., Gupta, N.M.: Catalytic and redox properties of nano-sized $La_{0.8}Sr_{0.2}Mn_{1-x}Fe_xO_{3-d}$ mixed oxides, *J,Mol. Catal. A-Chem.l,* **246**,128 – 135, (2006).

8 Shuang, Z., Shao-Yu, M., Zhao-Xiong, X., Lan-Sun, Z.: Preparation and gas sensing properties of Fe-doped yttrium manganate nanoparticles, *Sensor. Actuat. B-Chem.*, **156**, 23 – 27, (2011).

9 Bonet, A., Travitzky, N., Greil, P.: Synthesis of $LaCrO_3$ and $La_{0.9}Ca_{0.1}CrO_3$ by modified glycine nitrate process, *J. Ceram. Sci. Tech.*, **5**, 93 – 100, (2014).

10 [Pawar, M.J., Chaure, S.S., Deshmukh, S.B.: Effect of co codoping on the electrical conductivity of $Ce_{0.9}Sm_{0.1}O_{2-\delta}$, *J. Ceram. Sci. Tech.,* **1**, 27 – 31, (2010).

11 Romero, M., Faccio, R., Martínez, J., Pardo, H., Montenegro B., Plá Cid, C.C., Pasa, A.A., Mombrú, A.W.: Effect of lanthanide on the microstructure and structure of Ln-$Mn_{0.5}Fe_{0.5}O_3$ nanoparticles with Ln=La, pr, nd, sm and gd prepared by the polymer precursor method, *J. Solid State Chem.*, **221**, 325 – 333, (2015).

12 Pechini, M.P.: US Patent, **3**, 330 – 697, (1967).

13 Kakihana, M., Arima, M., Nakamura, Y., Yashima, M., Yoshimura, M.: Spectroscopic Characterization of Precursors Used in the Pechini-Type Polymerizable Complex Processing of Barium Titanate, *Chem. Mater*., **11**, 438 – 450, (1999).

14 Karen, P., Kjekshus, A.: Citrate-gel synthesis in the Y(O)-Ba(O)-Cu(O) system, *J. Am. Ceram. Soc.*, **77**, 547 – 552, (1994).

15 Kakihana, M., Milanova, M.M., Arima, M., Okubo, T., Yashima, M., Yoshimura, M.: Polymerized complex route to the synthesis of pure $Y_2Ti_2O_7$ at 750 C using Y:Ti mixed-metal citric acid complex, *J. Am. Ceram. Soc.,* **79**, 1673 – 1676, (1996).

16 Ekstrom, L., Olin, A.: On the complex formation between lead (II) and citrate íons in acid, neutral and weakly alkaline solution, *Chem. Scripta*, **13**, 10 – 15, (1978).

17 Todorovsky, D., Getsova, M., Vasileva, M.A.: Thermal decomposition of lanthanumtitanium citric complexes prepared from ethylene glycol medium, *J. Mater. Sci.,* **37**, 4029 – 4039, (2002).

18 Mazaki, H., Yasuoka, H., Kakihana, M., Fujimori, H., Yashima, M., Yoshimura, M.: Complex susceptibilities of Co-substituted $YBa_2Cu_3O_{7-d}$ synthesized by the polymerixed complex method, *Physica C,* **246**, 37 – 45, (1995).

19 Ertl, G., Knözinger, H., Weitkamp, J.: Preparation of solid catalysts, John Wiley & Sons, New York, 1992.

20 Sinquin, G., Petit, C., Hindermann, J.P., Kiennemann, A.: Study of the formation of $LaMO_3$ (M=Co, Mn) perovskites by propionates precursors: Application to the catalytic destruction of chlorinated VOCs, *Catal. Today,* 70, 183, (2001).

21 Arima, M., Kakihana, M., Nakamura, Y., Yashima, M., Yoshimura, J.: Polymerized complex route to barium titanate powders using barium-titanium mixed-metal citric acid complex, *J. Am. Ceram. Soc*., **79**, 2847 – 2856 (1996).

22 Hennings, D., Mayer, W.: Thermal decomposition of (BaTi) citrate into barium titanate, *J. Solid State Chem.*, **26**, 329 – 338, (1978).

23 Kumar, S., Messing, G.L., White, W.B.: Metal organic resin derived barium titanate. I, formation of barium titanium oxycarbonate intermediate, *J. Am. Ceram. Soc.*, **76**, 617 – 624, (1993).

24 Duran, P., Capel, F., Tartaj, J., Gutierrez, D., Moure, C.: Heating-rate effect on the $BaTiO_3$ formation by thermal decomposition of metal citrate polymeric precursors, *Solid State Ionics*, **141**, 529 – 539, (2001).

25 Nakamoto, K.: Infrared and raman spectra of inorganic coordination compounds, John Wiley & Sons, New York, 2009.

26 Liang, L., Xu, Y., Hou, X., Wu, D., Sun, Y., Li, Z., Wu, Z.: Small-angle x-ray scattering study on the microstructure evolution of zirconia nanoparticles during calcination, *J. Solid State Chem.,* **179**, 959 – 967, (2006).

[27] Guo, X., Gutsche, A., Wagner, M., Seipenbusch, M., Nirschl, H.: Simultaneous SWAXS study of metallic and oxide nanostructured particles, *J. Nanopart. Res.,* **15**, 1559, (2013).

[28] Pabisch, S., Feichtenschlager, B., Kickelbick, G., Peterlik, H.: Effect of interparticle interactions on size determination of zirconia and silica based systems – A comparison of SAXS, DLS, BET, XRD and TEM, *Chem. Phys. Letters,* **521**, 91 – 97, (2012).

[29] Kohn, W., Sham, L.J.: Self-consistent equations including exchange and correlation effects, *Phys. Rev. A.,* **140**, 1133, (1965).

[30] Hohenberg, P., Kohn, W.: Inhomogeneous electron gas, *Phys. Rev. B.,* **136**, 864, (1964).

[31] Parr, R.G., Yang, W.: *Density-functional theory of atoms and molecules,* Oxford University Press, 1989.

[32] Becke, A.D.: A new mixing of hartree-fock and local density-functional theories, *J. Chem. Phys.,* **98**, 5648, (1993).

[33] Perdew, J.P., Chevary, J.A., Vosko, S.H., Jackson, K.A., Pederson, M.R., Singh, D.J., Fiolhais, C.: Atoms, molecules, solids, and surfaces: Applications of the generalized gradient approximation for exchange and correlation, *Phys. Rev. B.,* **46**, 6671, (1992).

[34] Hay, P.J., Wadt, W.R.: *Ab initio* effective core potentials for molecular calculations, *J. Chem. Phys.,* **82**, 270 – 283, (1985).

[35] Frisch, M.J. *et al.*: Gaussian, Inc., Wallingford CT, 2009.

[36] Hammouda, B.: A new Guinier-Porod model, *J. Appl. Cryst.,* **43**, 716 – 719, (2010).

[37] Oliver, B.G., Davis, A.R.: Vibrational spectroscopic studies of aqueous alkali metal bicarbonate and carbonate solutions, *J. Inorg. Nucl. Chem.,* **34**, 2851 – 286, (1972).

[38] Kumar, S.: Raman study of ferric perchlorate and nitrate in acidic solutions, *J. Inorg. Nucl. Chem.,* **35**, 3831 – 3836, (1973).

[39] Hernández, M.T., González, M.: Synthesis of resins as alpha-alumina precursors by the pechini method using microwave and infrared heating, *J. Eur. Ceram. Soc.,* **22**, 2861 – 2868, (2002).

[40] Xu, Y., Yuan, X., Huang, G., Long, H.: Polymeric precursor synthesis of $Ba_2Ti_9O_{20}$, *Mater. Chem. Phys.,* **90**, 333 – 338, (2005).

[41] Petrova, N., Todorovsky, D.: Thermal decomposition of zirconium-yttrium citric complexes prepared in ethylene glycol and water media, *Mater. Res. Bull.,* **41**, 576 – 589, (2006).

[42] Vivekanandhan, S., Venkateswarlu, M., Satyanarayana, N.: Effect of ethylene glycol on polyacrylic acid based combustion process for the synthesis of nano-crystalline nickel ferrite ($NiFe_2O_4$), *Mater. Lett.,* **58**, 2717 – 2720, (2004).

[43] Pontes, F.M., Galhiane, M.S., Santos, L.S., Petit, L.A., Kataoka, F.P., Mabuchi, G.H., Longo, E., Zampieri, M., Pizani, P.S.: Polymeric precursor method to the synthesis of XWO(4) (X = Ca and Sr) thin films-structural, microstructural and spectroscopic investigations, *J.Alloy. Compd.,* **477**, 608 – 615, (2009).

[44] Farhikhteh, S., Maghsoudipour, A., Raissi, B.: Synthesis of nanocrystalline YSZ (ZrO_2-$8Y_2O_3$) powder by polymerized complex method, *J. Alloy. Compd.,* **491**, 402 – 405, (2010).

[45] Yang, W., Chang, Y., Huang, S.: Influence of molar ratio of citric acid to metal ions on preparation of $La_{0.67}Sr_{0.33}MnO_3$ materials via polymerizable complex process, *J. Eur. Ceram. Soc.,* **25**, 3611 – 3618, (2005).

[46] Wang, S., An, Y., Zhang, C., Zhang, Z., Qian, Y.: Ethanothermal reduction to MoO_2 microspheres via modified pechini method, *J. Cryst. Growth,* **293**, 209, (2006).

[47] Nishizawa, H., Katsube, M.: Preparation of $BaTiO_3$Thin films using glycolate precursor, *J. Solid State Chem.* **131**, 43 – 48, (1997).

[48] Rossiter, W.J., Godette, M., Brown, P.W., Galuk, K.G.: Investigation of the degradation of aqueous ethylene glycol and propylene glycol solutions using ion chromatography, *Sol. Energ. Mater.,* **11**, 455 – 467, (1985).

[49] Rosário, A.V., Pereira, E.C.: The effect of composition variables on precursor degradation and their consequence on Nb_2O_5 film properties prepared by the pecchini method, *J. Sol-Gel Sci. Technol.,* **38**, 233 – 240, (2006).

[50] Barton, D.H.R., Ollis, W.D.: Comprehensive organic chemistry: the synthesis and reactions of organic compounds, Oxford, Pergamon Press, 1979.